Computing uncertainties in ionosphere-airglow models: I. Electron flux and species production uncertainties for Mars

Guillaume Gronoff,[1] Cyril Simon Wedlund,[2] Christopher J. Mertens,[1] and Robert J. Lillis[3]

Received 11 June 2011; revised 14 January 2012; accepted 9 February 2012; published 5 April 2012.

[1] The ionization and excitation of atoms and molecules in the upper atmospheres of the Earth and planets are computed by a number of physical models. From these calculations, quantities measurable by dedicated satellite experiments such as airglow and electron fluxes can be derived. It is then possible to compare model and observation to derive more fundamental physical properties of the upper atmospheres, for example, the density as a function of altitude. To ensure the accuracy of these retrieval techniques, it is important to have an estimation of the uncertainty of these models and to have ways to account for these uncertainties. The complexity of kinetic models for computing the secondary production of excited state species (including ions) makes it a difficult evaluation, and studies usually neglect or underestimate it. We present here a Monte-Carlo approach to the computation of model uncertainties. As an example, we studied several aspects of the model uncertainties in the upper atmosphere of Mars, including the computed secondary electron flux and the production of the main ion species. Our simulations show the importance of improving solar flux models, especially on the energy binning and on the photon impact cross sections, which are the main sources of uncertainties on the dayside. The risk of modifying cross sections on the basis of aeronomical observations is highlighted for the case of Mars, while accurate uncertainties are shown to be crucial for the interpretation of data from the particle detectors onboard Mars Global Surveyor. Finally, it shows the importance of *AtMoCiad*, a public database dedicated to the evaluation of aeronomy cross section uncertainties. A detailed study of the resulting emissions cross sections uncertainties is the focus of a forthcoming paper (Gronoff et al., 2012) in which the outputs discussed in the present paper are used to compute airglow uncertainty, and the overall result is compared with the data from the SPICAM UV spectrometer onboard Mars Express.

Citation: Gronoff, G., C. Simon Wedlund, C. J. Mertens, and R. J. Lillis (2012), Computing uncertainties in ionosphere-airglow models: I. Electron flux and species production uncertainties for Mars, *J. Geophys. Res.*, *117*, A04306, doi:10.1029/2011JA016930.

1. Introduction

[2] Modeling the upper atmosphere of Earth and the planets has always been a challenge; in particular, accurately reproducing observations of both density and compositional variations. Other topics of interest include climate evolution and coupling to the solar wind. In this paper, we will focus on requirements for accurate remote sensing of atmospheric composition and density. Specifically, we will consider a forward model for remote sensing of the upper atmosphere.

[3] Forward models compute a parameter that we are able to observe, but which also depends on the parameter(s) we want to retrieve. Our forward model simulates radiance measurements, which depend on atmospheric state variables such as temperature, density and composition. Remote sensing techniques are based on adjusting the atmospheric state variable of interest until the simulated radiance computed by the forward model matches the observation. When the match is accomplished, the state variable is considered retrieved.

[4] Several standard techniques currently exist for the remote sensing of upper atmospheres [*Meier*, 1991]. One technique is the observation of stellar occultations. In this case, the absorption of stellar light is directly proportional to the column amount of intervening gas composition absorbed by the light (with some possible subtleties, for example when the absorption cross section is dependent on the temperature as in [*Forget et al.*, 2009]). Another widely used technique to study the mesosphere (for example, with the SABER instrument on NASA/TIMED [*Mertens et al.*, 2009]), is to retrieve atmospheric state variables from infrared and airglow emission along the limb line-of-sight. Compared to Earth's atmosphere,

[1]Chemistry and Dynamics Branch, Science Directorate, NASA Langley Research Center, Hampton, Virginia, USA.
[2]Belgian Institute for Space Aeronomy (BIRA-IASB), Brussels, Belgium.
[3]Space Sciences Laboratory, University of California Berkeley, Berkeley, California, USA.

0148-0227/12/2011JA016930

there is relatively little data for other planets due the small number of planetary missions. However, recent developments in airglow models [see *Gronoff et al.*, 2012] have bolstered the possibility to retrieve upper atmosphere densities of planets, particularly Mars. Other models have been used to try to retrieve hot oxygen densities on Mars. As an example, *Chaufray et al.* [2009] used the 1304Å oxygen line limb observation to retrieve hot oxygen densities in the upper atmosphere of Mars.

[5] The main weakness in using airglow models for the retrieval of upper atmosphere parameters is the presence of possibly large uncertainties. In some cases, these uncertainties can be large enough to render the technique impractical. Another disadvantage is the possibility of non-negligible contributions from unknown sources of emission. On the other hand, retrieval techniques for airglow emission have the major advantage of global coverage, which is very important for climatological studies and understanding the complex coupling between atmospheric altitude regions and their associated temporal variations. Therefore, in this series of papers, we concentrate on airglow emission forward models for use in remote sensing from limb observations. We attempt to overcome the main deficiency of this technique by conducting a detailed error analysis of a state-of-the-art airglow model, *Aeroplanets*, with application specific to Mars. This analysis is a necessary step to characterize uncertainties in the retrieved parameters and will also highlight our fundamental understanding of chemical, kinetic, and radiative processes.

[6] Airglow comes from the radiative de-excitation of excited-state neutral and ionized species. The first step to compute the airglow is therefore to compute the production of these states. The production can come from chemical reactions, which is studied in more detail in Part II [*Gronoff et al.*, 2012], but it is mainly due to charged particle and photon impact on neutral species, resulting in different atomic processes: ionization, dissociation, excitation, etc., depending on photon/particle energy and the impacted species. In the present paper, we concentrate on the physical sources of the excited state species at the origin of the airglow. Since the ionization creates secondary electrons which are energetic enough to efficiently excite species in the thermosphere, the study of the electron flux, and of its uncertainties, is a necessary step. It involves the use of an electron transport code, which is capable of computing the electron flux and the production of excited states species by electron impact (some of which cannot be created by photon impact). As in situ measurements of the electron flux can be made, comparisons with observations are possible at this stage of the work and can show the limitation of the current models—notably for the solar flux [e.g. *Jain and Bhardwaj*, 2011]—used in ionosphere-airglow models.

[7] The remainder of this paper is as follows: In section 2, we present the *Aeroplanets* model. We explain the computation of the excited species production, and we study the sources of uncertainties. We also introduce *AtMoCiad*, a cross section database developed to compute uncertainties. In section 3, we explain the Monte-Carlo technique used to compute the uncertainties. Finally, in section 4, we apply this technique to study the uncertainties in the computation of ion production and electron flux in the upper atmosphere of Mars. We compare the results with the measurements made by the Mars Global Surveyor Electron Reflectometer (MGS ER), and we present faster techniques to compute the uncertainties.

2. Ionosphere-Airglow Models: The Example of *Aeroplanets*

2.1. The *Aeroplanets* Model

[8] This coupled ionosphere-airglow model basically computes the production of excited state species by photon and electron impact, and calculates the light emission from this production. Different computational schemes can be used, but for precision and speed optimization, electron transport computation through solution of the Boltzman equation is preferred.

[9] *Aeroplanets* is a model that computes the ionization, excitation, and airglow in the upper atmosphere of Earth and other planets, following that scheme for the computation of the electron impact. It is a complete restructuring and enhancement of the Trans* model series [*Lummerzheim and Lilensten*, 1994], which have been successfully used to study the excited species production and the airglow of Mars and Venus [*Simon et al.*, 2009; *Nicholson et al.*, 2009; *Gronoff et al.*, 2008], the giant planets, and the outer satellites [*Menager et al.*, 2010, and references therein].

[10] Another important application of *Aeroplanets* is the computation of the energy per ion-pair production of several gases on different planets [*Simon Wedlund et al.*, 2011] and especially their uncertainties. The computation of this energy has several applications: It allows accelerated estimation of ion productions when electron transport models are too slow for the application, and when the modeled value is compared to the experimental one, if available, it allows us to assess the quality of the cross section data set used. Large differences between these values highlights the fact that some inelastic cross sections are likely to be missing, or counted twice, in our database. The technique of computing the energy per ion-pair production uncertainties used in these previous studies is explained in detail in section 3.1. For the species used in the present study, the difference between the computed and the experimental energy per ion-pair production is within the modeled error bars. The resulting uncertainty computation results will therefore be very close to those of a "perfect" data set.

[11] The main enhancements of *Aeroplanets* compared to the Trans* model series are: (1) generalization of the code for easy adept ability to other planets, (2) computation of electron fluxes along magnetic field lines (as in *Gronoff et al.* [2009]), (3) the use of solar flux grids not constrained to the *Torr and Torr* [1985] spectral grid, (4) computation of emissions along satellite line-of-sight field-of-view, and (5) the estimation of uncertainties through Monte-Carlo simulation. In addition, the Atomic and Molecular Cross sections for Ionization and Aurora (or Airglow) Database (*AtMoCiad*) has been developed and will soon be publicly available. The purpose of this database is to provide up-to-date cross sections, with the ability to facilitate their dissemination among the user community for modeling comparison purposes and identifying the need for further laboratory measurements.

[12] The equations being solved in the core of the *Aeroplanets* model being common to the vast majority of the existing models, and the physical inputs that can cause uncertainties being common to all the models, the following study of

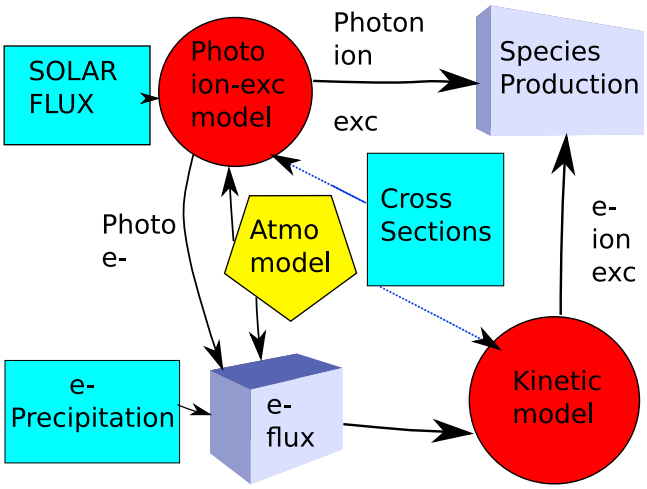

Figure 1. The *Aeroplanets* model workflow for the computation of the production of ionized and excited species. The rectangular blue boxes correspond to the model parameters, for which uncertainties can affect the retrieval accuracy. The yellow pentagon corresponds to the parameter that can be fitted. The red circles correspond to the computational parts, and the lavender 3-D boxes correspond to the outputs.

the uncertainty propagation can be considered as quite general and can apply to other models.

2.2. Principles of Computation

[13] In its standard mode of operation, *Aeroplanets* computes photoionization, photodissociation, and photoexcitation rates, secondary electron flux coming from photoelectrons, and subsequent electron-impact ionization, dissociation, and excitation rates. These quantities are used to calculate excited electronic states of species and their volume emission rates (VER), if applicable. The emissions rates are integrated to compute limb radiances. It is also possible to add the ion and electron production rates due to cosmic rays and high-energy protons, computed with *Planetocosmics* [*Gronoff et al.*, 2011]. In the near future, a fluid model will be added to compute the ion and electron densities, and their corresponding temperatures.

[14] The main *Aeroplanets* input parameters are the thermosphere-ionosphere ion and neutral densities and their associated temperatures, the solar flux, and the interaction cross sections. Some additional inputs are the geometry of the satellite line-of-sight field-of-view, and localization parameters such as latitude, longitude, and solar zenith angle (SZA).

[15] Figure 1 represents the workflow for the computation of the excited state production by *Aeroplanets*. The solar flux, the electron precipitation spectrum, the atmosphere model and the cross sections are the main inputs. Each are sources of uncertainties depending on the use of the model. For example, for retrieval, the atmosphere model can be considered as an output and therefore does not contribute to uncertainties. The two models, photoionization-excitation and kinetic (electron transport), use these inputs to compute their respective excited states production rates. The output of the photon transport model is also used in the determination of the electron flux at each altitude.

[16] In Figure 2, we show the workflow explaining how to process the produced excited states to compute the emission intensity observed by satellite instruments. The production of excited states is used directly to compute the VER in the case of allowed transition, and a geometric solver is used to integrate the emission along the satellite line-of-sight. For forbidden transitions, a chemical equilibrium approximation is assumed, which depends on the atmospheric density, but also the chemical reaction rates and the Einstein coefficient for emission. The output of this chemical module is the volume emission rate which can be integrated for satellite observation simulation. Since the *Aeroplanets* model is not yet coupled with a multiple-scattering radiative transfer model, it is only applicable to weak line radiation transfer scenarios (opacity $\tau < 1$, since it is possible to account for simple absorption through a Beer-Lambert law).

2.3. The Input Parameters

2.3.1. The Thermosphere-Ionosphere Model

[17] One of the main inputs to *Aeroplanets* is the thermosphere model, which gives the neutral temperature and densities as a function of altitude at a specified location.

[18] Another important input is the ionosphere model, which consists of the electron density and temperature needed to compute the Coulombian losses of energy of the suprathermal electrons. The ion composition and temperature are also necessary inputs, which can be extremely important for computing the emissions. These parameters can be computed with an ionization-excitation ionosphere model like *Aeroplanets* when coupled with a fluid module. Unfortunately, the magnetic field configuration can modify strongly the outputs of such models, and it is not recommended to use them for retrieval purposes. Therefore, the ion and electron densities and temperatures should be a parameter to be retrieved by remote sensing. It is necessary to make an initial "guess" of these inputs to estimate their relative importance and the uncertainty on the outputs due to these species. It typically implies to use a model for these parameters, and to make a perturbation of a factor (e.g. two) to check if the influence is minor or not.

[19] As an example, the electron recombination with O_2^+ creates hot oxygen, O(^1D) and O(^1S) excited states, which emit

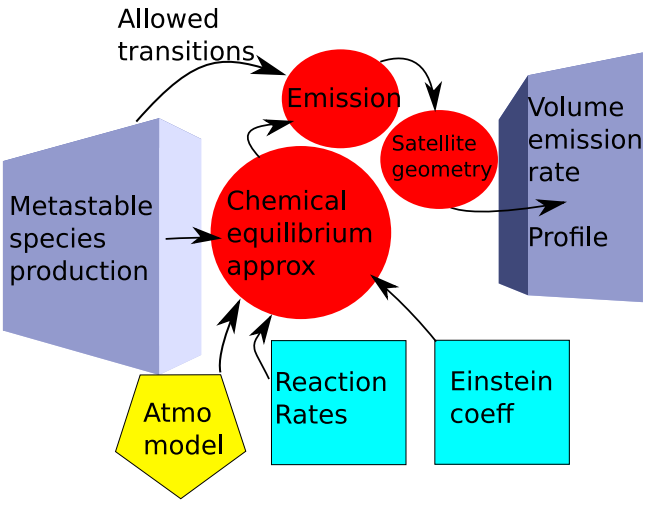

Figure 2. The *Aeroplanets* model workflow for the computation of emissions.

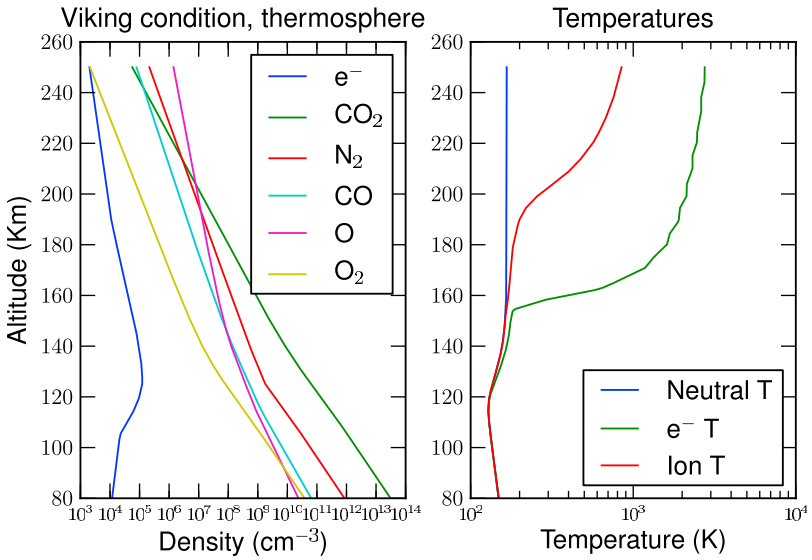

Figure 3. (left) The thermosphere model, including the electron density, and (right) the ionospheric model (electron and ion temperature; neutral temperature) for Mars in Viking conditions. This is the basic parameter to change from one planet to another.

the red and green lines, respectively, with a reaction rate depending on the electron temperature [*Mehr and Biondi*, 1969; *Gronoff et al.*, 2012]. Knowledge of the O_2^+ density, along with the ion temperature, is therefore necessary to compute the red and green line emissions. The addition of a fluid model, which computes the moments of the Boltzmann equation, enables the modeling of these ionospheric parameters. However, since the fluid model depends on outputs from *Aeroplanets* as well as on other parameters, it is also likely to have non-negligible uncertainties.

[20] For the Mars example, the ionosphere-thermosphere model is presented in Figure 3. This figure shows the neutral, electron and ion temperatures, as well as electron and neutral densities. It shows that the dominant constituent is CO_2 up to 200 km, which is then gradually replaced by O. It is based on the MTGCM [*Bougher et al.*, 2008] model for the neutral temperature and densities, which is able to reproduce the local atmospheric conditions observed by the Viking and Mariner missions [*Whitten and Colin*, 1974]. The electron and ion densities and temperatures are computed by the *TransMars* fluid model, (J. Lilensten, P.L. Blelly and O. Witasse, personal communication) that uses the *Bougher et al.* [2008] neutral atmosphere as input. The Bougher model also computes the electron density, and gives similar results as compared with *TransMars*.

[21] In the section below, we will consider the thermosphere-ionosphere state to be perfectly known (no associated uncertainties), and given by the MTGCM model. This will allow us to focus on the core of the model uncertainties, with the objective of determining the main sources of error in the forward model, which are the photon and electron-impact cross sections. We seek to understand the influence of these uncertainties on the retrieved thermospheric composition from limb emission observations.

2.3.2. Photon Impact Cross Sections

[22] The photon transport model, described in section 2.4, needs several inputs to compute the production of excited state species, and the light intensity at each altitude. First it needs the total absorption cross sections $\sigma_{h\nu}$ which determine the absorption by a species, and ultimately is used to compute the optical depth at each altitude. It also requires the partial production cross sections, $\sigma_{h\nu s}$, which determine the production of species *s*.

[23] Another important input is the solar flux, which is explained in detail in section 4.1.1.

2.3.3. Electron Impact Cross Sections

[24] The electron transport model described in section 2.5 is much more complex than the photoproduction model described in section 2.4. Moreover, additional input data is required, as described below:

[25] 1. The elastic scattering cross section $\sigma_{\epsilon el}$ determine the likelihood of the scattering event that does not alter the state of the impacted neutral. The direction of this scattering depends on the species, and is usually specified using the so-called Porter parameters [*Porter et al.*, 1987].

[26] 2. The inelastic $\sigma_{\epsilon inel}$ (non-ionizing) cross section determines the loss of energy of impacting electron, and the production of new species or excited states.

[27] 3. The (inelastic) ionization cross section, similar to the previous one, determines the loss of energy of the impacting electron and the production of ionized species, and also the creation of a new electron, whose energy is determined by some form of parameterization or measurement (see below).

[28] 4 The total cross section $\sigma_{\epsilon tot}$, the sum of the three previous, can be measured directly and may serve as reference.

[29] 5. The cross section for the production of secondary electrons $\sigma_{\epsilon sec}$ is used to determine the energy of an ejected electron (and hence the energy loss of the primary electron) and can be measured but is usually taken from a model (see section 2.5.2).

[30] The main ionization (i.e. the single ionization, and the ionization dissociation products in a case of a molecule) and total cross sections are typically well known, up to a precision of 5% [*Avakyan et al.*, 1998; *Straub et al.*, 1996]. The other inelastic cross sections (excitation, double ionization, K-shell ionization) are known to varying degrees of accuracy, depending on the species studied [see, for instance, *Simon Wedlund et al.*, 2011]. Unfortunately, because the elastic cross sections are

computed either by theory or by subtracting the inelastic (ionizing and non-ionizing) cross section from the total cross section, the uncertainty in this case is usually quite significant (more than 20%).

[31] To ensure the conservation of energy in electron transport models, it is important to have a comprehensive set of cross sections, the lack of such set is the principal limit of our computations. A technique to assure the quality of the cross section data, based on the computation of the energy per electron-ion pair production can be found in *Simon Wedlund et al.* [2011].

[32] To minimize the uncertainty in the computation of emission, it is preferable to use emission cross sections directly as compared to using excitation cross sections [*Johnson et al.*, 2005]. The physical reason is that the contribution to the emission also arises from cascading processes which depend on radiative, chemical and collisional deactivation of higher energy states. Using the measured emission cross section is less uncertain than combining those previous parameters, even if some experimental condition biases can appear, such as quenching in too dense conditions.

[33] Therefore, the *Aeroplanets* model uses emission cross sections when they exist and does not appear to have an excessive bias (measured for conditions of quenching, temperature, etc, that do not correspond to what will be encountered in the thermosphere).

2.3.4. The *AtMoCiad* Database

[34] To be able to compute uncertainties in the electron flux and the excited state production rates, we need the input model parameter uncertainties listed in the previous section. The input model uncertainties should be determined from a survey of the existing literature. Since a comprehensive database of the input model parameters' uncertainties does not exist, we have created the Atomic and Molecular Cross sections for Ionization and Aurora (or airglow) Database (*AtMoCiad*).

[35] The objective of *AtMoCiad* is to gather all the cross section data relevant for aeronomy and space plasma physics. The database is intended to be widely used and will be updated as necessary. Therefore, its user interface is based on two principles: open source files (*xml*) and an interactive web site to facilitate integrating new data.

[36] To be able to compare different experimental sources and legacy particle transport codes, it is important to maintain older data as well as new data. Therefore, for each input parameter, we include each available data set, along with their literature references. The database also includes a recommended "best estimate" for nominal use. This best estimate is calculated by interpolation between, and extrapolation from, the most reliable experimental and theoretical data sets. Choice of data sets and interpolation/extrapolation is based upon a combination of the age of the work, claimed uncertainties and literature recommendations.

[37] The claimed uncertainty is the primary factor used in the recommendation in the cross section parameter. *AtMoCiad* is a unique database as this information on input model parameters can be found nowhere else. The main problem in constructing this database is to estimate the uncertainty for theoretical data whose uncertainty comes from the approximations made in the models. However, this is not a problem exclusive to theoretical data since some of the legacy experiments lack uncertainty estimates as well.

[38] Another topic to consider in constructing the *AtMoCiad* database is energy grid extrapolation. For some input model parameters, it is important to have the cross section data cover the entire range of the transport model energy grid. But data points seldom go up to 2 keV. Therefore, extrapolations are made, typically log-log. However, the natural scatter in the lowest or highest few data points can result in unphysical extrapolations. One possible solution to this problem is to add new points, with a plausible value, a few hundred eV from the last data point. Typically, this does not affect most aeronomy codes, but it must be clearly explained. The second possible solution, found in the papers of *Shirai et al.* [2001, 2002]; *Tabata et al.* [2006], is to fit an analytical function to the data. Such analytical functions could reflect some basic physical processes and therefore provide physically plausible extrapolations.

[39] The *AtMoCiad* database is to be released online; additional information, including the references used for the creation of the database, will be provided at https://www.zotero.org/groups/atmociad.

2.4. Photon Transport Module

[40] The photoproduction module computes the production of excited state neutral species and ions due to the absorption of solar radiation. It also computes the photoelectron production which is necessary for the determination of the electron flux and the electron impact production of excited state species (section 2.5).

[41] In practice, if χ is the solar zenith angle (SZA), n_k the density of the neutral species k, and $\sigma^k_{h\nu}$ its total photoabsorption cross section, then the intensity of radiation at wavelength λ and altitude z is computed using the Beer-Lambert approximation [*Lilensten et al.*, 1989]:

$$I(\lambda, z) = I_\infty(\lambda) e^{-\tau(z,\lambda)}, \tag{1}$$

where the optical depth is given by:

$$\tau(z, \lambda) = \sum_k \sigma^k_{h\nu}(\lambda) \int_z^\infty n_k(z') \sec\chi(z') dz'. \tag{2}$$

For the transport of UV photons, in nonresonant cases, the dependence of the cross section $\sigma_{h\nu}$ on neutral temperature and altitude is negligible. Therefore the cross section is outside of the integral for the altitude in equation (2). This is not the case for infrared application.

[42] In the *Aeroplanets* model, the sec χ function has been modified to take into account the large χ, even greater than 90°. That modification is based on the formalism of the Chapman function [*Chapman*, 1931], modified for grazing angles [*Smith and Smith*, 1972], and without the hypothesis of an isothermal thermosphere in hydrostatic equilibrium [*Lilensten et al.*, 1989].

[43] Once the solar flux at each altitude is calculated, the production P_s of the species s is computed by:

$$P^k_s(\lambda, z) = n_k(z) \sigma^k_{h\nu s}(\lambda) I(\lambda, z) \tag{3}$$

$$P_s(z) = \sum_k \int_0^\infty P^k_s(\lambda, z) d\lambda. \tag{4}$$

With $\sigma^k_{h\nu s}$ the photoproduction cross section of species s from the photon impact on species k, P^k_s the s production from

photoimpact on k. We can see that there are two parameters driving the photoproduction uncertainty: (1) the photoabsorption cross section, which gives an uncertainty on the flux at each altitude and (2) the partial cross sections for production of each species.

[44] Therefore, if a species is produced through one photoionization channel, there are only two parameters to take into account to compute the uncertainties.

2.5. Electron Transport Module

[45] In addition to EUV solar photons, electrons, which can be precipitating electrons originating in the magnetosphere or secondary electrons from photon, electron, proton or cosmic ray impact, may be a significant source of excited states of atoms or molecules in the upper atmosphere. The bulk of the electrons in the ionosphere are thermalized, typically at temperatures in the 1000–2000 K range [*Witasse et al.*, 2008; *Withers*, 2009], which corresponds to Maxwellian energy distribution peaking at about 0.2 eV. These electrons are energetic enough to excite rotational-vibrational states, but, not to efficiently excite higher energy states (such as electronic states). The suprathermal electrons (those which have not undergone enough collisions to be thermalized) are the source of excitation of electronic states. The computation of excited species production by electron impact is much more complicated than the photoproduction and is classically described by Boltzmann's kinetic formalism [*Lilensten et al.*, 1990]. Upward and downward electron fluxes can be derived in the case of two-stream and multistream transport equations and be usefully compared to satellite data such as MGS for Mars.

[46] The electron flux Φ, that depends on altitude z, E (the energy of the suprathermal electrons), and μ (the pitch angle: cosines of the angle, see *Chandrasekhar* [1950]), is given by the Boltzman equation [e.g. *Schunk and Nagy*, 2004]:

$$\mu\frac{\partial\Phi}{\partial z} - n_e\frac{\partial}{\partial E}(L(E)\Phi) = -\sum_k n_k(z)\sigma^k_{\epsilon tot}(E)\Phi + S, \qquad (5)$$

where $L(E)$ corresponds to the Coulumb force (stopping power for e-e collisions), given by *Swartz et al.* [1971]:

$$L(E) = \frac{3.37\times10^{-12}}{E^{0.94}n_e^{0.03}}\left(\frac{E-T_e}{E-0.53T_e}\right)^{2.36} \qquad (6)$$

if n_e is the electron density in cm^{-3} and E and T_e, the electron temperature, are expressed in eV. S is a source term that includes the local production of electrons q, and the degradation in energy and modification of the angle of electron coming from different energies and angles. That degradation is characterized by the function R':

$$S(z,E,\mu) = q(z,E,\mu) \qquad (7)$$

$$+\int_E^\infty\int_{-1}^1 R'(E',\mu'\to E,\mu;z)\Phi(z,E',\mu')d\mu'dE'. \qquad (8)$$

[47] By introducing a discretization of energy in levels E_n, following an energy grid which can be optimized for energy conservation and $\Delta E_n = E_{n+1} - E_n$ the energy width of the grid at n, it is possible to replace the energy term in the left-hand side in equation (5) by:

$$\frac{\partial L(E)\Phi}{\partial E}\to\frac{L_{n+1}\Phi_{n+1}}{\Delta E_n} - \frac{L_n\Phi_n}{\Delta E_n}. \qquad (9)$$

The term just after the minus sign can be seen as a flux absorption, while the term before can be seen as a creation term.

[48] This permits us to introduce the opacity, in which a first part of the L(E) term is used (the other one will be used in equation (15)):

$$d\tau = -\left(n_e(z)\frac{L_n}{\Delta E_n} + \sum_k \sigma^k_{\epsilon tot}(E_n)n_k(z)\right)dz. \qquad (10)$$

[49] From that point, equations (5) and (8) can be expressed as a radiative transfer equation, for which several solvers exist [e.g. *Stolarski*, 1972; *Lummerzheim*, 1987; *Lilensten et al.*, 1990; *Lummerzheim and Lilensten*, 1994]:

$$\mu\frac{\partial\Phi}{\partial\tau} = \Phi - \frac{\omega}{2}\int p(\mu\to\mu')\Phi(\mu')d\mu' + Q, \qquad (11)$$

where p describes the angular redistribution and is similar to the phase function in classical radiation transfer theory, and Q is a newly defined source function which will be described in depth in section 2.5.2. The ω term is the albedo of elastic scattering. It corresponds to the albedo of single scattering in the classical radiative transfer equation, and is defined as:

$$\omega = \frac{\sum_k \sigma^k_{\epsilon el}(E_n)n_k(z)}{n_e(z)\frac{L_n}{\Delta E_n} + \sum_k \sigma^k_{\epsilon tot}(E_n)n_k(z)}. \qquad (12)$$

2.5.1. Redistribution in Angle

[50] Because *Aeroplanets* is a multistream code, an angle-by-angle solution of equation (5) is performed, which allows not only better precision in simulating the suprathermal electron flux distribution, but also allows the backscattered electron pitch angle distribution to be analyzed [*Lillis et al.*, 2008] in cases when magnetic mirror effects can be neglected (for magnetic analysis, equation (5) and the solver must be modified, see the mathematical formulation in [*Lummerzheim*, 1987]). Magnetic mirror effects can be quite safely ignored for electrons produced at or near the ionization peak as the magnetic field does not change by an appreciable amount over their mean free path. However, [*Lillis et al.*, 2009] showed that magnetic mirror effects are important for calculating production rates when both of the following conditions are satisfied: 1) the precipitating electrons are at least moderately anisotropic in pitch angle and 2) the fractional increase in magnetic field from the electrons' "initial" altitude to the exobase is >30%. Therefore, in the case of particle precipitation above even modest Martian crustal magnetic field anomalies, results need to be interpreted carefully. It is the intention to include magnetic mirror effects in this model framework in future.

[51] In *Aeroplanets*, the electrons created by photon and electron impact are assumed to be isotropically distributed in angle. For the impacting electron in inelastic collisions, the direction is assumed to be unchanged by the collision [*Porter et al.*, 1987]. For elastic collisions, the redistribution in angle

cannot be neglected, and therefore must be parameterized. In *Aeroplanets*, this is done through the *Porter et al.* [1987] parameterization at low energy, and with the Rutherford parameterization (which is a boundary of the Porter function) at high energy (>500 eV).

[52] The p function corresponds to the redistribution in angle after an elastic impact collision. These redistributions were studied experimentally by *Porter et al.* [1987]. Because there is no privileged direction in the atmosphere for the redistribution in angle, we can consider the function $p(\mu'')$ where μ'' corresponds to the angle between μ and μ'. If a magnetic field is strong enough and has a gradient strong enough to create magnetic mirroring then this approximation breaks down and a term depending on the angle relative to the direction of the magnetic field arises. But we will ignore this complication in the present paper because for most of planetary atmospheres, it can be neglected below the exosphere. Therefore $p(\mu'')$, which has the angular form of a screened Rutherford elastic scattering cross section [*Porter et al.*, 1987], is specified by:

$$p(\mu'') = \frac{1}{N}\left[\frac{1}{(1+2\gamma-\mu'')^2} + \frac{\beta}{(1+2\delta-\mu'')^2}\right] \tag{13}$$

$$N = \frac{1}{4}\left[\frac{1}{\gamma(1+\gamma)} + \frac{\beta}{\delta(1+\delta)}\right]. \tag{14}$$

The β, γ, and δ are the Porter parameters. They are measured for each species, and are the main source of uncertainty for the redistribution in angle (if the discretization in angle is important enough).

2.5.2. Redistribution in Energy

[53] The source function Q of equation (11) is defined by:

$$Q = q_n + n_e\Phi_{n+1}\frac{L_{n+1}}{\Delta E_n} + \sum_{i=n+1}^{N} R_{in}\Phi_i. \tag{15}$$

Recall that q_n is the creation of electrons from the ionization processes. For the photoionization case, the energy ascribed to the secondary electron is $E_{\text{photon}} - E_{\text{threshold}}$ where E_{photon} is the incident photon energy and $E_{\text{threshold}}$ is the ionization potential. If an Auger electron is created, its energy is precisely defined, simplifying the computation. For simplicity, we have suppressed the angular dependence in q_n and Φ.

[54] As an example, the q_n part due to the photoionization is written:

$$q_n(z, E_n, \mu) = \frac{1}{4\pi}\sum_{\lambda,k,s} P_k^s(\lambda, z)\delta\left(E_n, \frac{hc}{\lambda} - E^s_{\text{threshold}\,k}\right), \tag{16}$$

$$\text{with}\,\delta(E_n, E) = 1\,\text{if}\,E\,\text{is inside the}\;E_n\;\text{box} \tag{17}$$

$$\delta(E_n, E) = 0\;\text{else} \tag{18}$$

For this equation, h is the Planck constant, c the speed of light, and it is valid only if one electron is ejected. The production, $P_k^s(\lambda, z)$, is computed from equation (3). The $\frac{1}{4\pi}$ comes from the hypothesis of isotropic redistribution in angle.

[55] R_{in} represents the formation of an electron with energy E_n from the degradation of electron with energy E_i and is given by (see also appendix A):

$$R_{in} = \frac{\sum_k(\sigma^k_{\epsilon inel}(E_i \to E_n) + \sigma^k_{\epsilon sec}(E_i \to E_n)\Delta E_n)n_k(z)}{n_e(z)\frac{L_n}{\Delta E_n} + \sum_k \sigma^k_{\epsilon tot}(E_n)n_k(z)}. \tag{19}$$

The first term in the numerator, $\sigma^k_{\epsilon inel}(E_i \to E_n)$, is the inelastic cross section that accounts for the energy degradation of the impact electron (from E_i to E_n). This cross section has units of cm^2. The source of the energy degradation cross section of the impact electron is from the measurement database described in section 2.3.4. The remaining unknown quantity in computing these interactions is the final energy state of the degraded impact electron, which we describe below. The energy degradation of the impact electron, $\sigma^k_{\epsilon inel}(E_i \to E_n)$, is the sum of two processes. The first energy loss process is due to excitation (non ionization) of the target neutral particle. By energy conservation $E_n + W = E_i$, where W is the energy excitation of the electronic state. The second energy degradation process for the impact electron is due to energy carried away by the creation of a secondary electron. By energy conservation, $E_n + W_I + E_s = E_i$, where E_s is the energy of the secondary electron, and W_I the ionization threshold.

[56] The second term in the numerator, $\sigma^k_{\epsilon sec}(E_i \to E_n)$, is also an inelastic cross section that accounts for the creation of a secondary electron at energy E_n from an impact electron at energy E_i, and is a differential cross section ($\frac{\partial\sigma}{\partial E_n}$, with units of $\text{cm}^2\ \text{eV}^{-1}$). The energy spectrum of the secondary electron can be very large, with the exception of Auger electrons, which are better described as tertiary electrons. A doubly differential cross section is needed to account for their energy. These cross sections, $\sigma_{\epsilon sec}$, depend on the energy of the impacting electron and their measurement are limited to energies of the impacting electron below 2 keV. Therefore, theoretical results must be combined with the measurements in order to obtain these cross section in the energy range needed for the computation. We used the theoretical parameterization from *Rees et al.* [1969] and *Opal et al.* [1971], which are described in more detail below.

[57] The *Rees et al.* [1969] approximation is based on first-order Born approximation cross section calculations combined with an oscillator strength fit on measurements.

[58] The Rees parameterization for the doubly differential cross sections is given by:

$$\sigma^k_{\epsilon sec}(E_i \to E_n) = \frac{1}{N}\sigma^k_{ger} \times \Gamma^k \tag{20}$$

$$\Gamma^k = \ln\frac{\sqrt{E_i} + \sqrt{E_i - E_n - W_I^k}}{\sqrt{E_i} - \sqrt{E_i - E_n - W_I^k}} \tag{21}$$

$$\sigma^k_{ger}(E_i \to E_n) = \frac{\exp(-\alpha_R E^k_{nI} - \beta_R\exp(-\gamma_R E^k_{nI}))}{E^k_{nI}} \tag{22}$$

$$E^k_{nI} = E_n + W_I^k \tag{23}$$

$$\alpha_R = \frac{1}{31.5} \tag{24}$$

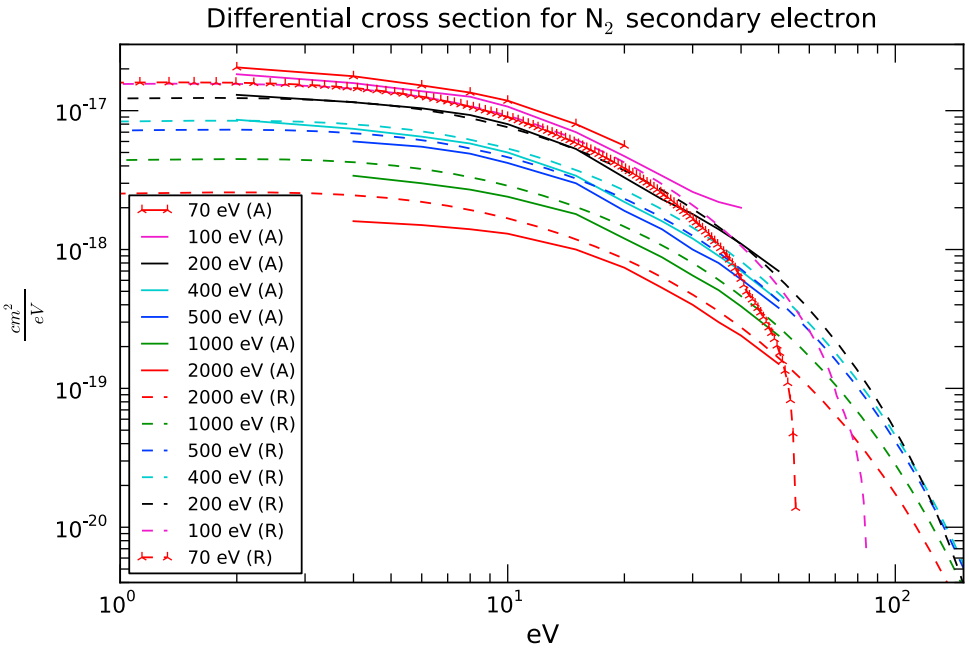

Figure 4. The differential cross section for the secondary electron production by electron impact on N_2. In the model the cross sections marked (R) were computed using the *Rees et al.* [1969] formulae and are compared to the measured cross sections in *Avakyan et al.* [1998], marked (A).

$$\beta_R = 339 \tag{25}$$

$$\gamma_R = \frac{1}{2.49} \tag{26}$$

$$\frac{1}{N} = \frac{\sigma_{ioni}(E_i)}{\int_0^{E_i} \sigma^k_{ger}(E_i \rightarrow E_n) dE_n}. \tag{27}$$

This formulation was derived from measurements fitted to an N_2, O_2, O atmosphere, with a 20% accuracy. Comparison between this function and actual measurements are shown in Figure 4 for N_2 at various electron impact energies. This cross section parameterization is a good approximation for Earth, but must be used with caution for other planets like Mars, for which the atmosphere is different. The main problem with this cross section specification is that it is difficult to vary the parameters according to the target species (except the $\sigma_{ioni}(E_i)$ in the renormalization factor; equation (27)).

[59] The *Opal et al.* [1971] parameterization for the $\sigma^k_{esec}(E_i \rightarrow E_n)$ is given by:

$$\sigma^k_{ger}(E_i \rightarrow E_n) = \frac{1}{1 + \left(\frac{E_n}{E^k_p}\right)^{2.1}} \tag{28}$$

$$\sigma^k_{esec}(E_i \rightarrow E_n) = \frac{1}{N} \sigma_{ger}, \tag{29}$$

where E_p is a parameter determined from the experiment for each species, and the normalization factor $\frac{1}{N}$ is computed as in the previous parameterization. In this case, the accuracy is also 20%, similar to the Rees parameterization. The advantage of the Opal parameterization is that the E_p parameter has been fitted to a wider range of target species, making the extension to other planetary atmospheres more reliable. In *Aeroplanets*, both parameterizations are included, but because of the advantage of the Opal parameters for other planets, it is nominal to use equation (29).

[60] In Figure 5, we plot the comparison between the measurements in *Avakyan et al.* [1998] and the doubly differential cross section computed with the *Opal et al.* [1971] parameter E_p. The error bars in the figure show the influence of 5% uncertainty in the E_p parameter, but does not show the corresponding uncertainty in the normalization constant. The uncertainty in the normalization constant must be taken into account in the actual computation of the electron spectrum.

2.5.3. Solving the Problem

[61] Equation (11) defines a system of radiative transfer equations, one for each energy in the grid, that must be solved from the highest energy to the lowest. For each energy, the flux Φ is solved through the routine "DISORT" (DIScrete Ordinate method for Radiative Transfer [*Stamnes et al.*, 1988]). This approach is possible because equation (5) is in the form of a radiative transfer equation, with the addition of a derivative in energy. The boundary conditions are dependent on the problem: for the present vertical case, the electron flux at the top of the altitude grid is fixed (at 0 when precipitation are not taken into account), and the flux at the bottom of the grid is totally reflected (the altitude grid must be defined to avoid a large reflection). For other cases, e.g. the computation along magnetic field lines [*Gronoff et al.*, 2009], it is possible to consider that the "bottom" flux is absorbed, simulating an escape of electrons.

[62] The routine "DISORT" can easily propagate the rounding errors and the other computational uncertainties due to the discretization and due to mathematical approach of the solver. To check the stability of the solution, energy conservation is computed and maintained as explained in *Lummerzheim and*

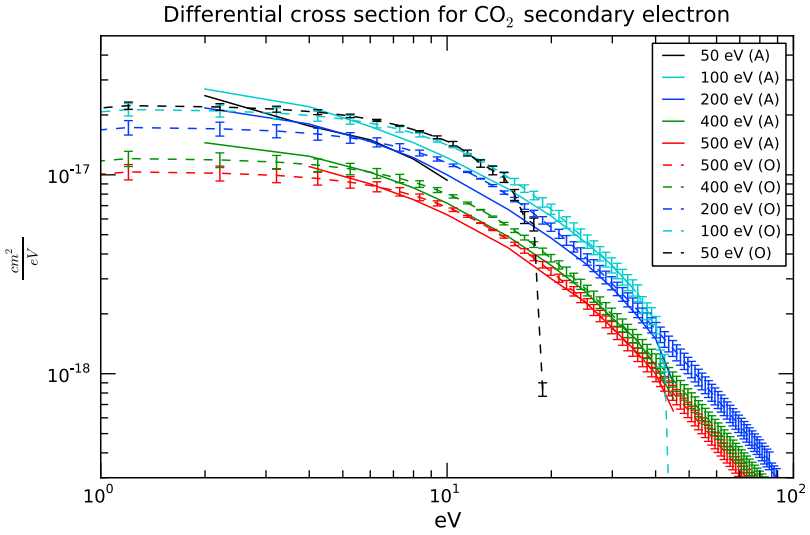

Figure 5. The differential cross section for the secondary electron production by electron impact on CO_2. In the model the cross sections marked (O) were computed using the *Opal et al.* [1971] formulae and are compared to the measured cross sections in *Avakyan et al.* [1998], marked (A). In the model the E_p parameter was perturbed with an intensity of 5%, giving us the represented error bars. In the actual computation another uncertainty coming from the cross section, which influences the renormalization parameter, must be taken into account.

Lilensten [1994]. Therefore, it is possible to estimate the computational uncertainties for the model, typically the model errors are on the order of 5%. A careful choice of energy grid enables quasi-perfect energy conservation (see appendix B).

[63] Once the electron transport equation has been solved, equation (5), the production rate of the excited state s by electron impact, is given by:

$$P_s(z) = \sum_k n_k(z) 2\pi \int_{-1}^{1} \int_0^{\infty} \sigma_{es}^k(E') \Phi(z, E', \mu) dE' d\mu'. \quad (30)$$

Similar to the photoproduction rate in equation (3), the cross section above can be different than the one used in computing the R matrix, equation (19), therefore, we can use emission cross sections directly rather than combining electronic states excitation cross sections and spontaneous emission rates, the combination of which can lead to larger uncertainties.

2.5.4. The Advantages of the Multistream Approach

[64] A number of standard electron transport algorithms are based on the two-stream approximation, which assumes an isotropic electron spectrum in the upward and the downward hemispheres. However, in the presence of non-vertically aligned magnetic fields, the absorption path can be 10 times longer than an hemispheric average over an isotropic distribution. For example, the multistream *Aeroplanets* model was able to accurately calculate the electron fluxes on Titan in the presence of a non-vertically aligned (Saturn's) magnetospheric magnetic field [*Gronoff et al.*, 2009]. On the other hand, a two-stream electron transport code would have significantly underestimated the electron fluxes on Titan.

2.5.5. The Total Production

[65] The total production of an electronic excited state is the sum of the production by photon and electron impact. Other sources of excitation such as proton impact, galactic cosmic rays, or meteoritic ionization can be present, but are usually dominant at altitudes below the ionosphere-thermosphere. The total production rates are ultimately used to compute radiative emissions of the excited states, or the state populations in a fluid model.

[66] The contribution of the excited state production rates uncertainties to the radiative emissions uncertainties are discussed in *Gronoff et al.* [2012].

2.6. The Model Limitations

[67] The study of the physics of the code shows us that two kinds of uncertainties can arise: (1) the computational model uncertainties (approximations in solving the transport, resolution of the spectral and energy grids, etc), and (2) the input model uncertainties. The former can be minimized by imposing constrains such as conservation in energy, described in B, and can therefore be considered negligible in comparison with the latter. The main input parameters determining the uncertainties of *Aeroplanets* are the cross sections (including $L(E)$), the Porter parameters, the oscillator strength for the redistribution in energy (equations (28)–(29)), the solar flux and the electron precipitation spectrum. For emission, it is also important to take into account uncertainties in chemical reaction rates (an issue that is addressed in *Gronoff et al.* [2012]).

[68] The input parameter uncertainties listed above should not be confused with model uncertainties [*Bevington and Robinson*, 2003]. Model uncertainties arise from physical processes that have been neglected, but may be important under certain conditions.

[69] Such neglected processes are:

[70] 1. The radiative transfer of the Ly_α radiation in the photoproduction module: the resonant scattering is not taken into account but may be important. Solar resonant scattering may also be important at other wavelengths (for instance for λ1304 O I, λ1356 O I, etc.).

[71] 2. The effect of the internal sources of radiations in the photoproduction module (e.g., Auger photons do not ionize in the model).

[72] 3. Thermal emissions are neglected: this is only a problem for IR study, and for hypothetical exoplanetary atmospheres.

[73] 4. Non-dependence of the cross sections on the local conditions (temperature, pressure, etc). This is mainly a problem for IR studies, but cases exist where it should be taken into account for UV studies [*Forget et al.*, 2009].

[74] 5. Electron scattering in non-forward directions by inelastic collisions.

[75] 6. Non-isotropic production of secondary electrons after ionization.

[76] 7. Steady state equilibrium assumption. This may break down near the terminator.

[77] 8. Magnetic mirror effects.

[78] 9. The uncertainties in the input ionosphere and thermosphere models.

[79] 10. The other sources of ionization (protons, cosmic rays).

[80] 11. The geometry of the model (1D, plane-parallel, or following the magnetic field line), which is not applicable for horizontally inhomogeneous media.

3. Computing the Uncertainties

[81] Several approaches are possible to estimate the uncertainties of a model, based on the uncertainties of its parameters. For models with only a few parameters, it is possible to directly modify the value of these parameters (of a 1-σ intensity for example), and to take the extreme values. This only works if we suppose a certain linearity in the perturbations by the different parameters. When the model exhibits nonlinearity, the simplest solution is to use the Monte-Carlo approach [*Bevington and Robinson*, 2003].

3.1. The Monte-Carlo Approach

[82] The Monte-Carlo approach consists in perturbing the different parameters with a random value, following a law depending on the uncertainties of that parameter. Typically, a Gaussian law is used, with σ equal to the claimed uncertainty of the parameter. This is the technique used in the following calculations.

[83] Several computations are then made varying these parameters, and the results are analyzed with the idea that the main perturbation of the results corresponds to the uncertainty of the model due to the parameter uncertainties.

[84] We find that each degree of freedom needs typically 30 simulations to adequately cover its range; and so, a correct simulation should be called a number of times to at least 30 to the power of degrees of freedom. For example, if we want to compute the photoproduction of CO_2^+ in a pure CO_2 atmosphere, we have two degrees of freedom, the CO_2 photoabsorption cross section, and the CO_2^+ production cross section, therefore $30^2 = 900$ runs are needed. In the same manner, if the atmosphere is composed of CO_2 and O, the photoabsorption of these two species have to be taken into account in addition to the production cross section. These three degree of freedom implies 27000 runs.

[85] If all the uncertainties wish to be taken into account in the computation of the emissions, several millions of computations are needed. With each run lasting about one minute, the simulation time would be too long. Therefore, we will compute which uncertainties can be neglected to reduce the number of simulations needed. To reduce the (user perceived) computation time, the Ciment Grid (CiGri) was used, allowing the use of several hundreds of processors in parallel. Moreover, with a step-by-step technique, it is possible to dramatically reduce the number of runs.

3.2. Treatment of the Results

[86] The variation of the different results for the perturbed run can be visualized in histograms, like in Figure 6, for which 900 launches of the *Aeroplanets* model were performed with different perturbations of the photoabsorption-ionization cross sections for each run. For this simulation, the CO_2 photoabsorption and the CO_2^+, CO^+, O^+, O_2^+ photoproduction cross sections have been perturbed, according to the uncertainties reported in the *AtMoCIAD* database. The other Martian species' uncertainties have been neglected for that simulation since their effect is orders of magnitude lower at the altitudes considered. Since the photoproduction uncertainties for CO_2^+, CO^+, O^+, and O_2^+, are independent, this system can be considered with two degrees of freedom for the computation. At each altitude, the histogram of production rates from these runs approximately follows a lognormal distribution. Therefore, we can fit a Gaussian to that histogram, whose parameters, the expected value μ' and the standard deviation σ', are related to the main value and the error (μ, σ) through the relations $\mu = \exp(\mu')$ and $\sigma = \mu \times \sigma'$ [*Bevington and Robinson*, 2003]. If we want to compute the uncertainties for the photoproduction of CO_2^+, the steps to follow are:

[87] 1. Launch the simulation, at least 900 times, with perturbation in the cross sections at each step.

[88] 2. Gather the data, take their logarithm, and for each altitude, compute an histogram.

[89] 3. Fit a Gaussian to each histogram.

[90] 4. Modify the Gaussian data to get the mean value and the uncertainties.

[91] With such a method, it is possible to compute the uncertainties in the model outputs due to the uncertainties in input parameters. As an example, we can see in Figure 7 the uncertainty in the photoproduction of the major ions in the Martian atmosphere. This figure is the result of the previous computation for which the uncertainties were analyzed for CO_2^+, CO^+, O^+, and O_2^+. The percent error is also plotted as a solid line (top axis). Interestingly, the uncertainty above the production peak is typically <30%, which is approximatively the square root of the sum of the squared errors of the photoabsorption and photoionization cross sections. Below the peak, the absolute uncertainties continue to increase with decreasing altitude as the rates rapidly decrease, resulting in much larger relative uncertainties.

4. Application to Mars

[92] The overall objective of sensitivity studies is to estimate the magnitude of the total uncertainty, and to know which parameters are at the origin of this uncertainty. One interesting piece of information is the relative importance of each parameters in the uncertainty: the computation of the overall uncertainty can by simplified by neglecting minor parameters. This could be useful to compute the uncertainty for different

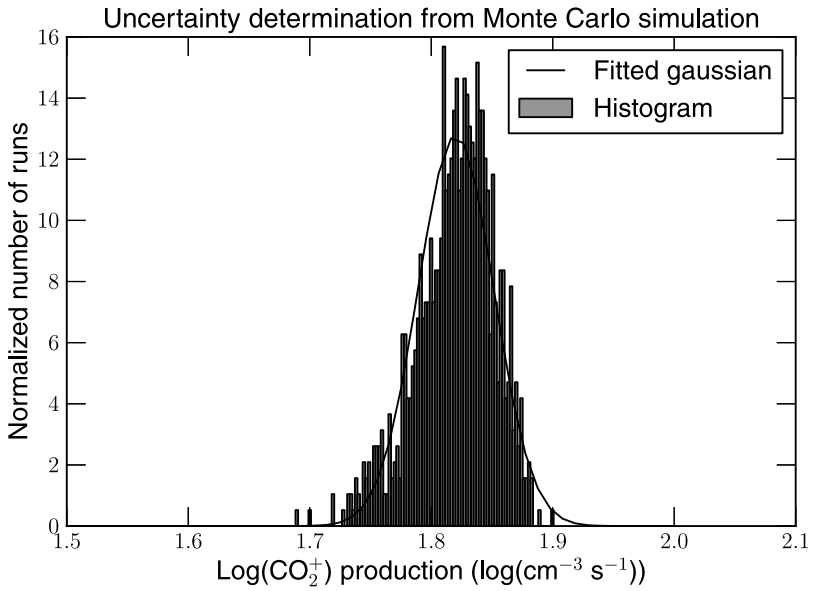

Figure 6. Histogram of the production of CO_2^+ at 150 km by photoproduction at Mars, for 900 launches, with a perturbation of the cross sections. The resulting Gaussian fit is analyzed, and its standard deviation is taken as the error in the production.

conditions of solar flux, electron precipitation, atmospheric composition, etc.

[93] In this section, we will compute the effect of each source of uncertainty by using the example of the Martian upper atmosphere ionization. From these computations, we will extract the main uncertainty parameters, and estimate what overall accuracy can be accepted.

[94] We will first study the influence of the solar flux model in comparison with electron flux data from MGS. Then, we will study in depth the model uncertainties impact on the electron flux, to highlight the main sources of uncertainties. And finally, we will study the impact on the production of excited state species.

[95] This work will test the capabilities of *Aeroplanets* in computing the productions uncertainties. These productions being necessary to compute the airglow, the output of the present computations is used in *Gronoff et al.* [2012].

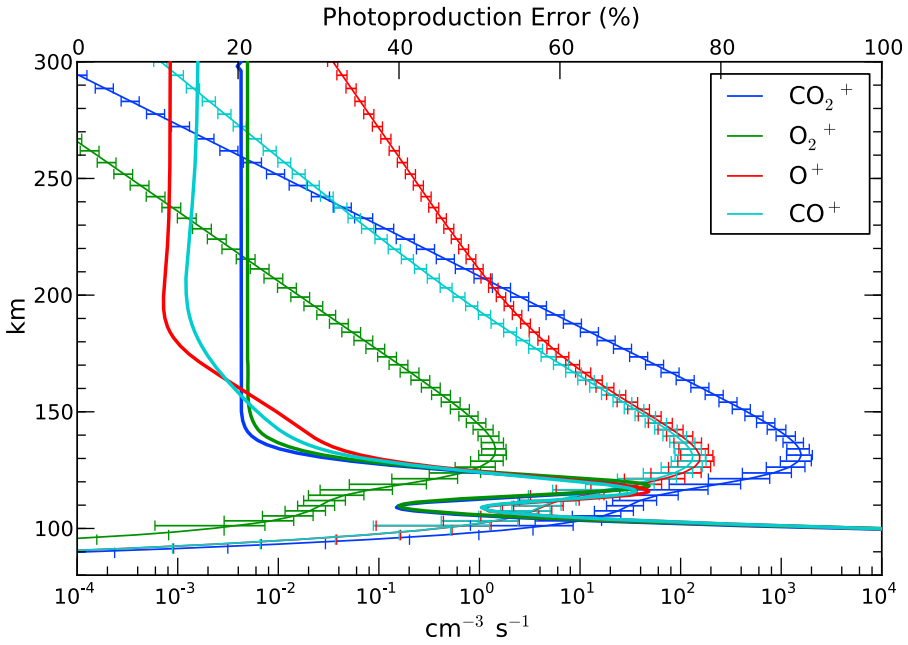

Figure 7. Photoproduction of CO_2^+ and other major Martian ions, with the error bars, resulting from the analysis described in Figure 6 at every altitude. The solid lines without the error bars correspond to the percentage error.

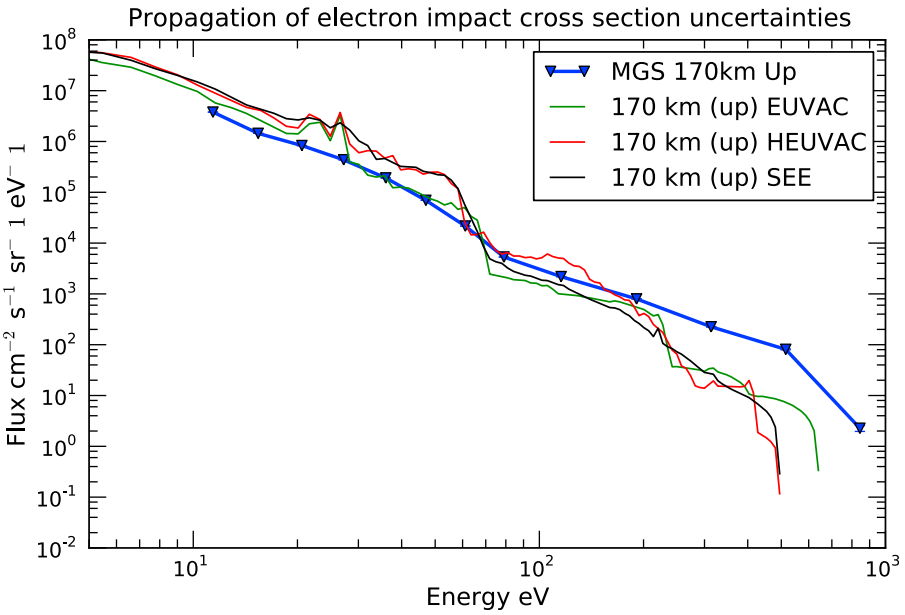

Figure 8. Upward electron fluxes observed by Mars Global Surveyor (MGS) at 170 km and modeled using *Aeroplanets* with different solar fluxes.

4.1. A Working Example

[96] To apply the modeling to a physical situation, we chose a test case corresponding to a MGS measurement of the electron flux, at quite low altitude (170 km) on the day side for solar zenith angles between 60° and 75°, with a weak (<25 nT) and mostly vertical magnetic field (magnetic elevation angle between 60° and 75°). These conditions allows us to neglect a) the precipitation of electrons from the solar wind (the photoelectrons are the dominant population of suprathermal electron in the dayside, at low altitude and with a weak magnetic field), b) magnetic mirroring (important for stronger magnetic fields) and c) retardation of electron vertical motion by the magnetic field (as would be the case if the field is not mostly vertical). These latter 2 effects cannot be simulated in the current code.

4.1.1. The Solar Flux Model and Its Uncertainties

[97] The main concern is the solar flux used, and the wavelength grid used in specifying the incident solar EUV-XUV flux at the top of the atmosphere. Initially, solar flux models such as EUVAC used the *Torr and Torr* [1985] 39 wavelength boxes some of them dedicated to isolated strong solar lines. Unfortunately, when better precision is needed to study the energy deposition above 100 eV (below 12.4 nm), these boxes are too wide and do not extend high enough in energy. As a result it is nearly impossible to study Auger ionization, and to compare it with observations [*Mitchell et al.*, 2000]. Moreover, if models such as *Aeroplanets* are to be adapted to exoplanets, these boxes, optimized for the sun, may become inadequate.

[98] To analyze that effect, we compared the electron flux in the upper atmosphere of Mars as computed by the *Aeroplanets* model with the MGS observations [*Mitchell et al.*, 2001] (Figure 8). Because we neglect the particle precipitation, this electron flux consists of the photoelectrons, the photoelectrons degraded in energy, and the secondary electrons produced by electron impact ionization, for which the cascade comes ultimately from a photoelectron. Therefore, the simulated electron flux is extremely sensitive to the solar flux model and can be used to compare each model's influence.

[99] The first model used is the EUVAC model [*Richards et al.*, 1994a, 1994b]. Because of the binning, the computed electron flux shows important bumps, for example at 70 and 240 eV. Because the electron energy grid used in the *Aeroplanets* model has a better resolution than the solar flux energy grid, the system however computes very precise features, like the Auger electron peak close to 220 eV (coming from the Auger excitation of the C atom in the CO_2 molecule).

[100] Then to improve the results, we used the HEUVAC model [*Richards et al.*, 2006]. Because this model gives the photon flux on a regular energy grid (0.1 nm and better), it is possible to interpolate the photon flux on the (finer) energy grid, without much error in the modification (the conservation in energy is better than 2%). This computational modification allows to have a smoother electron flux at high energy (greater than 200 eV), where the binning effects are strong. Thanks to that modification, the output electron flux appears more physically valid since it does not have the strong bump as when computed with EUVAC.

[101] Finally, to give a more physical value to the solar flux, the data of TIMED/SEE [*Woods et al.*, 2005] were used for the computation. We applied the same interpolation as for the HEUVAC model on these data. The resulting computation is smoother than that provided by HEUVAC.

[102] A comparison of the results of the three models shows that, even if computed for similar solar conditions in terms of $F_{10.7}$, the outputs are very different above 60 eV, with a ratio of up to five between EUVAC and HEUVAC at 110 eV. One possible explanation for that discrepancy is the variability of the solar flux above 100 eV, which is not efficiently parametrized by the $F_{10.7}$ proxy, and is highly variable [*Mitchell et al.*, 2000; *Woods et al.*, 2003]. Therefore, in the following analysis, we will use the actual solar flux data of SEE instead of the models.

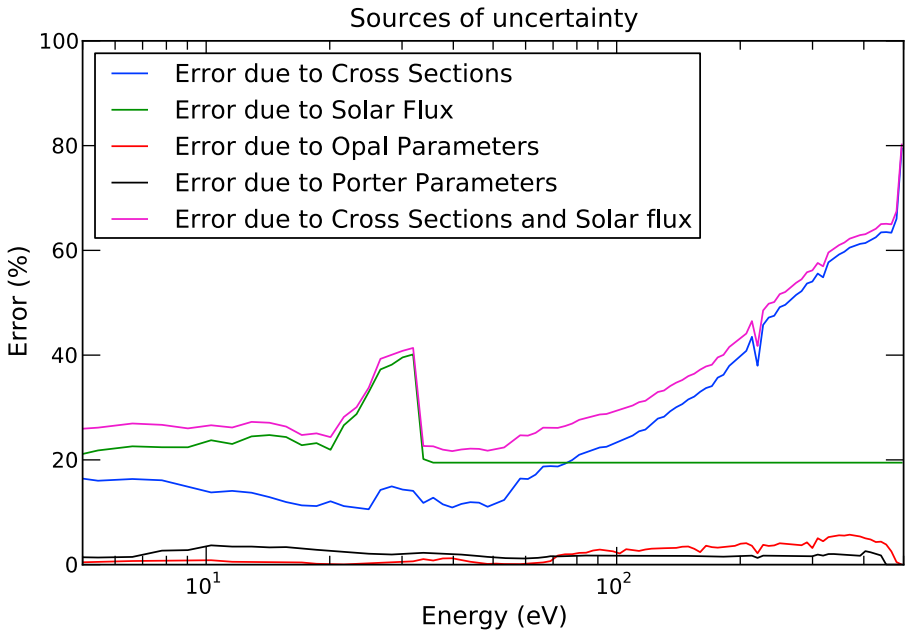

Figure 9. Electron flux uncertainties for each source, computed with *Aeroplanets*. For these simulations the SEE solar flux was used.

[103] This approach reflects the accuracy that will be possible with the MAVEN mission: The embedded UV radiometer is expected to give a solar flux with a precision better than 30% (F. G. Eparvier, personal communication, 2011).

4.1.2. Data-Model Comparison

[104] As can be observed in the different flux figures (Figures 8 and 11), the model-data agreement is reasonable at low energy (within a factor of 2) but has greater discrepancies at higher energies (>200 eV, with a factor of 10).

[105] These differences have several possible origins in addition to the uncertainties in the *Aeroplanets* model. The solar flux, as mentioned above, is highly variable above 100 eV (below 12 nm), and only an instrument in orbit aroud Mars could accurately reflect the variation of that input; unfortunately, such an instrument was not available for the MGS observations. Another important influence is the neutral atmosphere, which ultimately could be fitted to the data if the precision is sufficient. And finally, the precipitation of charged particles, neglected in the present computation, may be important in some cases.

4.2. Secondary Electron Flux Uncertainty

[106] To estimate the possible importance of the biases due to the neglected parameters and the solar flux, it is necessary to compute the model uncertainties. To do so, we study each influence one by one, and finally we estimate the overall uncertainty using the non-negligible ones.

4.2.1. Uncertainty Due to the Porter Parameters

[107] The first analysis comes from the study of the uncertainties of the Porter parameters. Since the main effect of these parameters is to modify the orientation of the scattered electrons, it is more likely to affect the upward-downward difference in the electron flux. The three parameters are perturbed by 10% of their value, which results in a 10% uncertainty in the differential cross section, close to the observed differences between the model and the measurements [*Porter et al.*, 1987].

[108] The resulting uncertainties can be seen in Figure 9, the highest value is lower than 4% for the electron flux at 10 eV.

4.2.2. Uncertainty Due to the Secondary Electron Energy Redistribution and the *L*(*E*) Function

[109] The second analysis concerns the secondary electrons, driven by the Opal (or Rees) parameters, and normalized by the ionization cross section. Since that cross section is just for the normalization, we considered only the perturbation of the Opal parameters. To obtain an uncertainty of 20% from the Opal parameters (see section 2.5.2), a variation of the Opal energy by 20% is sufficient.

[110] The effect on the flux is smaller at very low energy, with a 1% uncertainty at 10 eV, and is slightly greater, 5%, at 400 eV, as seen in Figure 9.

[111] Concerning the $L(E)$ function, a variation of 10% of its main parameter affects the fluxes and the production rates on the order of 10^{-3}%. The main effect of that parameter is on energy conservation, but the variation of conservation due to variation in photoelectron intensity is much higher. Unfortunately, the precision of the $L(E)$ parameter is not known, as the equation for $L(E)$ is a fit on a theoretical function [*Swartz et al.*, 1971]. The very small uncertainties from that parameter allows us to neglect its influence. However, further analysis, notably for the effect of heating, should reconsider more carefully the $L(E)$ uncertainties.

4.2.3. Uncertainty Due to the Elastic and Inelastic Electron-Impact Cross Sections

[112] The third analysis concerns the electron impact cross sections. For much of the species, the electron impact ionization is known with a 5% accuracy, and the main inelastic cross sections are known with 20% uncertainty. In the present computation, we used the uncertainties claimed by the authors for CO_2, as reported in AtMoCiad. The main sources of uncertainties are the ionization cross section, with a 5% uncertainty, and the $CO(a^3\Pi)$ production, with a 25% uncertainty. (This latter cross section is studied in detail in *Gronoff et al.* [2012].)

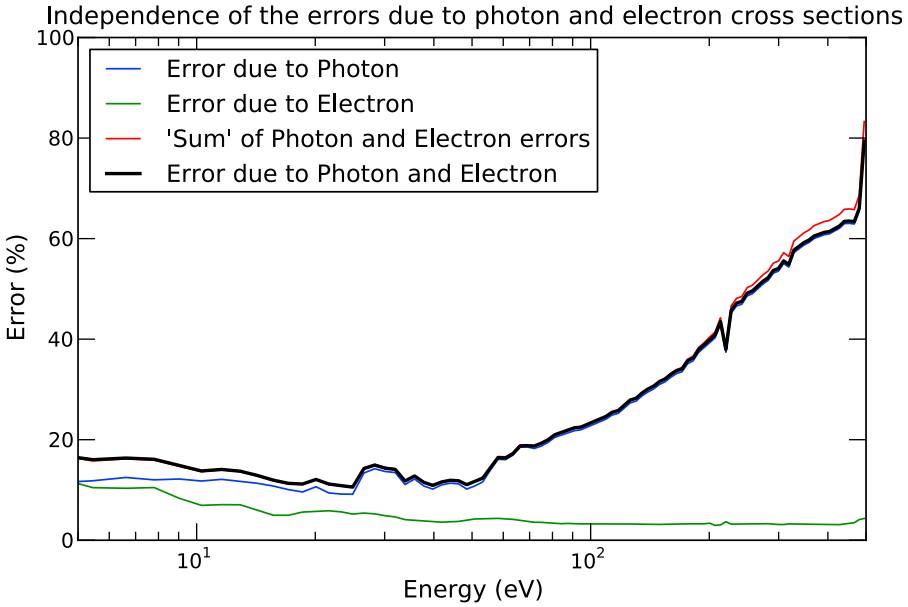

Figure 10. Uncertainties computed for the electron flux at 170 km. The blue curve corresponds to the errors when the photon cross sections are perturbed, the green curve to the errors when the electron cross sections are perturbed, and the black curve to the errors when both photon and electron cross sections are perturbed. The red curve corresponds to the square root of the sum of the square of the green and blue uncertainties; because it practically does not differ from the total uncertainties, we can conclude that the photon and electron uncertainties can be considered as independent, and therefore the number of simulations can be decreased.

[113] The resulting error propagation can be seen in Figure 10. For the modeled fluxes, the uncertainties are below 10% for energies >100 eV, below 15% in the 50–100 eV range, and below 25% elsewhere.

4.2.4. Uncertainty Due to the Photon Impact Cross Sections and the Photon Flux

[114] To complete the analysis of the electron production uncertainty, it is necessary to understand the propagation of the uncertainties of the photoelectron production. These uncertainties comes from the photoionization (and absorption) cross sections, which have been analyzed above (section 3.2). The resulting flux uncertainty can be seen in Figure 10. Typically, the uncertainties are in the 40%–70% range above 250 eV, between 20% and 40% in the 100–250 eV range, 15%–40% for 50–100 eV, and below 30% elsewhere.

[115] The other source of uncertainty for the primary photoelectron is the solar flux, which is not in itself a model parameter of *Aeroplanets* but an input. In some studies the secondary electron flux is even used to infer the input solar flux [*Woods et al.*, 2003; *Peterson et al.*, 2009]. The typical uncertainty in the measured solar flux is 20% [*Cessateur et al.*, 2011; *Woods et al.*, 2005], and directly reflects on the secondary electron flux. The solar flux uncertainty used in the computation was taken from the TIMED/SEE estimations. The result, in Figure 9, shows that this uncertainty is the most important below 70 eV, with a value varying in the 20%–40% range.

4.2.5. Model Uncertainties and Improved Computation Approach

[116] Overall, the value of these uncertainties shows that it is possible to totally neglect the uncertainties arising from the Porter and Opal parameters.

[117] To account for the cross sections and the solar flux uncertainties without too much computation, it is possible to study the independence of these parameters: in Figure 10 we plotted the error (in percentage) in the electron flux due to the electron impact cross sections, the photon cross sections, and the two of these combined. We also summed the photon and electron errors (by taking the square root of the sum of the square). That summed value being very close to the error when both types of cross sections are perturbed, we conclude that the errors can be considered independent. Moreover, we have a better idea of the magnitude of the uncertainties as a function of energy: in the 0–80 eV range, it may be necessary to take into account the electron impact uncertainties to have a better estimation of the overall uncertainty (since many of the excitation cross sections peak in that domain, this analysis is useful). Therefore, the independence of the parameters allows us to greatly simplify the computation of the uncertainty: we first compute the uncertainty due to the photon cross sections, then the one due to the electron impact cross sections. If we suppose that we have 2 main parameters for each cross section, it means that instead of 30^4 computations, only 2×30^2 are necessary. The exact same computation can be made with the solar flux (Figure 9), and therefore, the computation of the whole uncertainty can be made with less than 2000 simulations.

[118] This uncertainty computation allows us to compare the model with the data in Figure 11. Below 80 eV, the MGS downward electron flux (for which we plotted the shot noise) is inside the error bars of the model. In contrast, the modeled upward electron flux is twice the observed flux. More generally, over the whole energy range, the computed upward flux is twice as much as the computed downward flux. This is believed to be an atmospheric effect: simulations at lower altitude, i.e. higher density, shows the two fluxes with similar values.

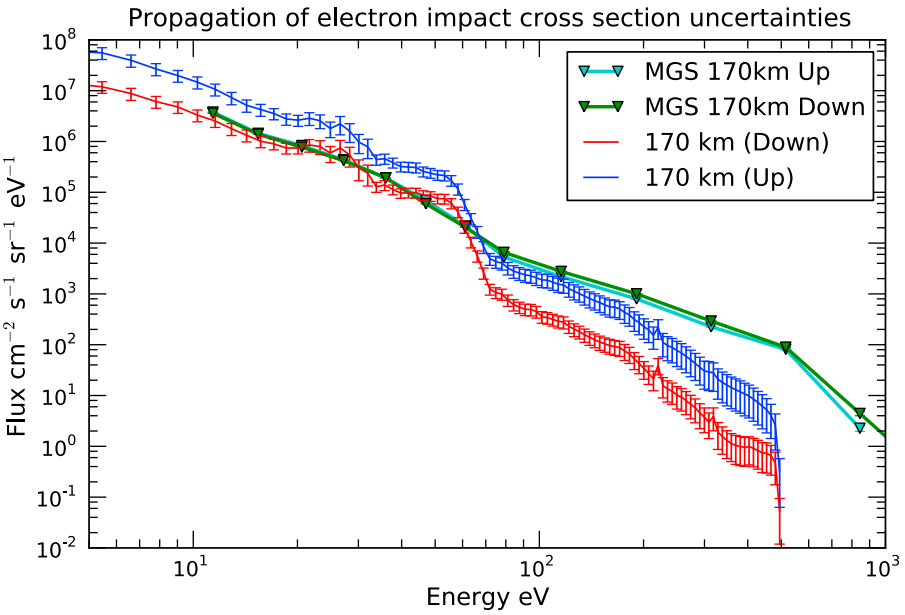

Figure 11. Comparison of the electron flux computed by *Aeroplanets* with the measurements by MGS. The main sources of uncertainties, from the cross sections and the solar flux, have been taken into account. The discrepancy between the model and the data at low energy can come from the neutral atmosphere, while at high energy, other precipitation sources, including more energetic photons, may be necessary to explain the discrepancy.

Above 80 eV, the computed downward electron flux is much lower than the observed one, and the explanation comes probably from the solar flux intensity, though electron precipitation cannot be rejected.

4.3. Excited State Species Production

[119] The computation of the excited state species production is important as an input for chemical, fluid, and/or airglow models.

4.3.1. Cross Section Uncertainties

[120] Figure 12 allows us to sum up the result for dayside ionization uncertainty computation. The production of the main species are plotted with their respective error bars when electron impact cross section are perturbed (left) and when photon cross sections are perturbed (right).

[121] The amplitude of the uncertainty due to the photon impact cross sections (right) is much more important than the electron impact ones (left) for ion production. Besides the large photoionization cross section uncertainties, it is to be noted that the photon cross sections have a double influence on the uncertainty: they directly influence the photoproduction, but they also create of a perturbation of the photoelectron flux which results in a modification of the electron impact production. This case does not generalize for all the excited state species production: Some excited states are produced mainly by electron impact, with uncertainties above 20% [see *Gronoff et al.*, 2012].

4.3.2. Solar Flux and Total Uncertainties

[122] Figure 13 shows the influence of the solar flux uncertainty on the ion production. In the left panel, only the solar flux uncertainties are taken into account, while in the right panel, solar flux and cross sections uncertainties are computed together.

[123] As for the electron flux in section 4.2.5, it is possible to combine the cross section uncertainties with the solar flux uncertainties to retrieve the total uncertainties: An uncertainty combination analysis would give results similar to those shown in Figure 10.

[124] The results of the computations presented in Figures 12 and 13 show that the current limitations in the computation of ion production comes from both the solar flux model and the photon impact cross sections. An interesting result for future missions to Mars is that above the production peak, one can expect accuracy better than 30% with the current data.

4.3.3. Species Production Uncertainty

[125] With the independence of the cross section uncertainties established, it is possible to compute uncertainties for all the physical productions for the different excited state species. The production can be integrated in chemical models to obtain the density of different ion species, and in radiative transfer models to obtain the emissions. A study of the propagation of the uncertainties in these models is the focus of *Gronoff et al.* [2012].

5. Summary and Conclusion

[126] In this paper (Part I), we have described the *Aeroplanets* model, which computes ionization and emissions in planetary atmospheres. We have also described the Monte-Carlo technique to estimate the uncertainties. Through a detailed analysis of the different sources of uncertainties, we have determined that the solar flux and photon and electron impact cross sections are the main sources of uncertainties for the production of the different species, both ions, as shown here, and other states, as presented in Part II [*Gronoff et al.*, 2012]. For the ion production, we have shown that the total

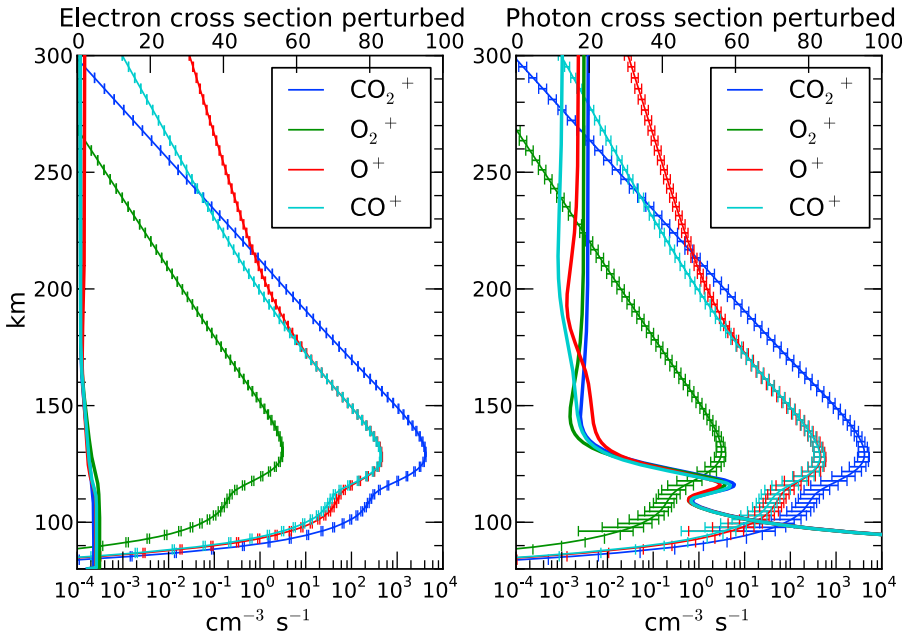

Figure 12. Production of CO_2^+, and other major Martian ions by photon and electron impact. In the left panel, only the electron impact cross sections were perturbed. In the right panel, only the photoionizations (and photoabsorptions) cross sections were perturbed.

uncertainties are about 25% above 150 km, due to both uncertainties in the cross sections and the solar flux, and much more important below 150 km with a sharp increase at the peak altitude, due mainly to uncertainties in the cross sections. Moreover, these uncertainties are found to be independent, and it is possible to greatly reduce the number of model computations in order to obtain an adequate estimation of these uncertainties.

[127] The computed magnitude of the uncertainties shows the importance of efforts to experimentally and theoretically determine the different cross sections, especially the photoionization-photoabsorption cross sections. The

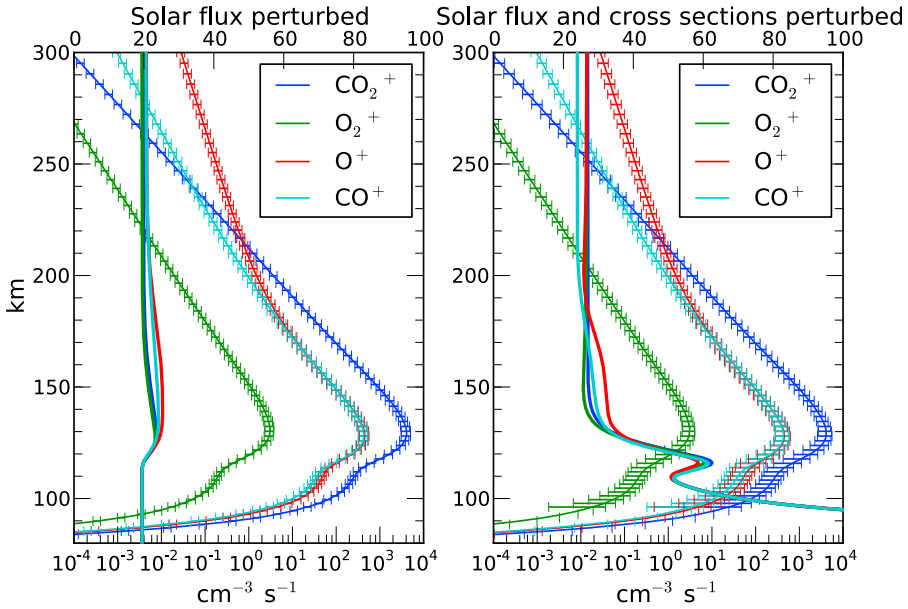

Figure 13. Production of CO_2^+, and other major Martian ions, with the error bars, taking into account the solar flux uncertainties. In the left panel, only the solar flux was perturbed, leading to an uncertainty proportional to that perturbation. In the right panel, the photon and electron cross sections were also perturbed. A comparison of these results with those in Figures 7 and 12 shows that the total error corresponds to the square root of the other errors squared. Such a relationship allows a simple computation of the total uncertainties when the induced errors of the cross section are known.

coming *AtMoCiad* database will help to emphasize the most important cross sections and will improve the collaboration not only between different teams (chemists, aeronomers, etc.) but also between observer, experimentalists, and modelers.

Appendix A: The Redistribution Matrix *R* and the Auger Electrons

[128] The R_{in} function is dimensionless. In *Lummerzheim* [1987], it has the dimension of the inverse of an energy, and in the summation, there is a multiplication by the grid width. Since the dimension of (non-doubly differential) cross sections is a surface, and not a surface divided by the energy (as for the doubly differential), one has to divide the cross section by the width of the boxes to have a correct R expression. For clarity reasons we preferred the expression independent of the energy. However, when the energy is discretized, one must be very careful with the different width for the energy grids, especially when degrading energy from one large box to smaller boxes. To that extent the *Lummerzheim* [1987] approach is better suited to the practical computation.

[129] This point must be taken into account for the computation of the Auger electron production. Auger electrons are different from the usual secondary electron because of their defined energy. Therefore, there is no need for Ress or Opal parameterization for the creation of these electrons. If σ_{eAuger} is the cross section for the creation of an Auger electron of energy E_{Auger}, equation (19) can be rewritten:

$$R_{in} = \frac{\sum_k (\sigma^k_{einel}(in) + \sigma^k_{esec}(in)\Delta E_n + \sigma^k_{eAuger}(i)\delta(E_{Auger}, E_n))n_k(z)}{n_e(z)\frac{L_n}{\Delta E_n} + \sum_k \sigma^k_{etot}(E_n)n_k(z)} \tag{A1}$$

(with the notation $\sigma(in)$ corresponding to $\sigma(E_i \rightarrow E_n)$ and $\sigma(i)$ to $\sigma(E_i)$).

Appendix B: The Energy Conservation

[130] The energy deposition rate is the sum of the energy rate absorbed by the target species through inelastic impact Q_a, and the heating of the electron gas Q_e [*Lummerzheim and Lilensten*, 1994].

[131] The electron gas heating rate Q_e is computed by [*Schunk and Nagy*, 1978]:

$$Q_e(z) = \int_{E_t}^{\infty} L(E)\Phi_T(E)dE + \left(E_t - \frac{3}{2}kT_e\right)L(E_t)\Phi_T(E_t). \tag{B1}$$

In the above equation, E_t is the energy where the thermal distribution of the electron is equal to the suprathermal flux, and Φ_T is the angular-integrated flux. The energy absorption rate is computed by:

$$Q_a(z) = \sum_k n_k(z) \int_0^{\infty} \sum_s W^k_s \sigma^k_{es}(E)\Phi_T(E)dE. \tag{B2}$$

Therefore, after integration over the altitudes, we must have:

$$Q_i = \int\int q_i(E,\mu)d\mu dE = Q_d = Q_a + Q_e. \tag{B3}$$

Nominally, we require Q_i to be equal to Q_d within 5%.

[132] **Acknowledgments.** The authors are in debt to Jean Lilensten (IPAG, France), and Arun Gopalan (SSAI/NASA, USA) for useful discussions, and also to Ryan Norman (NASA, USA) for the long hours discussing the philosophy of the energy grid uncertainties. The authors wish to thank the anonymous referees for their numerous comments, suggestions, and corrections. The work of Guillaume Gronoff was supported by an appointment to the NASA Postdoctoral Program at NASA Langley Research Center, administered by Oak Ridge Associated University through a contract with NASA, and funded by the NASA Science Mission Directorate. The work of Rob Lillis was funded by NASA Mars Fundamental Research Program grant NNX09AD43G and the NASA Mars Data Analysis Program grants NNX08AK94G and NNX11AI87G.

[133] Robert Lysak thanks the reviewers for their assistance in evaluating this paper.

References

Avakyan, S. V., R. llin, V. Lavrov, and G. N. Ogurtsov (1998), *Collision Processes and Excitation of Ultraviolet Emission From Planetary Atmospheric Gases: A Handbook of Cross Sections*, 344 pp., Gordon and Breach, Amsterdam, Netherlands.

Bevington, P. R., and D. K. Robinson (2003), *Data Reduction and Error Analysis for the Physical Sciences*, 3rd ed., 320 pp., McGraw-Hill, Boston, Mass.

Bougher, S. W., P. Blelly, M. Combi, J. L. Fox, I. Mueller-Wodarg, A. Ridley, and R. G. Roble (2008), Neutral upper atmosphere and ionosphere modeling, *Space Sci. Rev.*, *139*(1-4), 107–141, doi:10.1007/s11214-008-9401-9.

Cessateur, G., T. D. de Wit, M. Kretzschmar, J. Lilensten, J. Hochedez, and M. Snow (2011), Monitoring the solar UV irradiance spectrum from the observation of a few passbands, *Astron. Astrophys.*, *528*, A68, doi:10.1051/0004-6361/201015903.

Chandrasekhar, S. (1950), *Radiative Transfer*, *Int. Ser. Monogr. Phys.*, 393 pp., Clarendon, Oxford, U. K.

Chapman, S. (1931), The absorption and dissociative or ionizing effect of monochromatic radiation in an atmosphere on a rotating earth, *Proc. Phys. Soc.*, *43*, 26–45.

Chaufray, J. Y., F. Leblanc, E. Quémerais, and J. L. Bertaux (2009), Martian oxygen density at the exobase deduced from O I 130.4-nm observations by spectroscopy for the investigation of the characteristics of the atmosphere of Mars on Mars Express, *J. Geophys. Res.*, *114*, E02006, doi:10.1029/2008JE003130.

Forget, F., F. Montmessin, J. L. Bertaux, F. González-Galindo, S. Lebonnois, E. Quémerais, A. Reberac, E. Dimarellis, and M. A. López-Valverde (2009), Density and temperatures of the upper Martian atmosphere measured by stellar occultations with Mars Express SPICAM, *J. Geophys. Res.*, *114*, E01004, doi:10.1029/2008JE003086.

Gronoff, G., J. Lilensten, C. Simon, M. Barthélemy, F. Leblanc, and O. Dutuit (2008), Modelling the Venusian airglow, *Astron. Astrophys.*, *482*, 1015–1029, doi:10.1051/0004-6361:20077503.

Gronoff, G., J. Lilensten, and R. Modolo (2009), Ionization processes in the atmosphere of Titan. II. Electron precipitation along magnetic field lines, *Astron. Astrophys.*, *506*, 965–970.

Gronoff, G., C. Mertens, J. Lilensten, L. Desorgher, E. Flückiger, and P. Velinov (2011), Ionization processes in the atmosphere of Titan. III. Ionization by high-*Z* nuclei cosmic rays, *Astron. Astrophys.*, *529*, A143, doi:10.1051/0004-6361/201015675.

Gronoff, G., C. Simon Wedlund, C. J. Mertens, M. Barthélemy, R. J. Lillis, and O. Witasse (2012), Computing uncertainties in ionosphere-airglow models: II. The Martian airglow, *J. Geophys. Res.*, doi:10.1029/2011JA017308, in press.

Jain, S. K., and A. Bhardwaj (2011), Impact of solar EUV flux on CO Cameron band and CO_2+ UV doublet emissions in the dayglow of Mars, *Planet. Space Sci.*, *63-64*, 110–122, doi:10.1016/j.pss.2011.08.010.

Johnson, P. V., I. Kanik, J. W. McConkey, and S. S. Tayal (2005), Collisions of electrons with atomic oxygen: Current status, *Can. J. Phys.*, *83*, 589–616.

Lilensten, J., W. Kofman, J. Wisemberg, E. S. Oran, and C. R. Devore (1989), Ionization efficiency due to primary and secondary photoelectrons – A numerical model, *Ann. Geophys.*, *7*, 83–90.

Lilensten, J., D. Fontaine, W. Kofman, L. Eliasson, C. Lathuillere, and E. S. Oran (1990), Electron energy budget in the High-Latitude ionosphere during Viking/Eiscat coordinated measurements, *J. Geophys. Res.*, *95*(A5), 6081–6092, doi:199010.1029/JA095iA05p06081.

Lillis, R. J., D. L. Mitchell, R. P. Lin, and M. H. Acuña (2008), Electron reflectometry in the Martian atmosphere, *Icarus*, *194*(2), 544–561, doi:10.1016/j.icarus.2007.09.030.

Lillis, R. J., M. O. Fillingim, L. M. Peticolas, D. A. Brain, R. P. Lin, and S. W. Bougher (2009), Nightside ionosphere of Mars: Modeling the effects of crustal magnetic fields and electron pitch angle distributions

on electron impact ionization, *J. Geophys. Res.*, *114*, E11009, doi:10.1029/2009JE003379.
Lummerzheim, D. (1987), Electron transport and optical emissions in the aurora, Ph.D. thesis, Univ. of Alaska, Fairbanks, Alaska.
Lummerzheim, D., and J. Lilensten (1994), Electron transport and energy degradation in the ionosphere: Evaluation of the numerical solution, comparison with laboratory experiments and auroral observations, *Ann. Geophys.*, *12*, 1039–1051, doi:10.1007/s00585-994-1039-7.
Mehr, F. J., and M. A. Biondi (1969), Electron temperature dependence of recombination of O_2^+ and N_2^+ ions with electrons, *Phys. Rev.*, *181*, 264–271.
Meier, R. R. (1991), Ultraviolet spectroscopy and remote sensing of the upper atmosphere, *Space Sci. Rev.*, *58*, 1–185, doi:10.1007/BF01206000.
Menager, H., M. Barthélemy, and J. Lilensten (2010), H Lyman α line in Jovian aurorae: Electron transport and radiative transfer coupled modelling, *Astron. Astrophys.*, *509*, A56.
Mertens, C. J., et al. (2009), Kinetic temperature and carbon dioxide from broadband infrared limb emission measurements taken from the TIMED/SABER instrument, *Adv. Space Res.*, *43*(1), 15–27, doi:10.1016/j.asr.2008.04.017.
Mitchell, D. L., R. P. Lin, H. Rème, D. H. Crider, P. A. Cloutier, J. E. P. Connerney, M. H. Acuña, and N. F. Ness (2000), Oxygen auger electrons observed in Mars' ionosphere, *Geophys. Res. Lett.*, *27*(13), 1871–1874, doi:200010.1029/1999GL010754.
Mitchell, D. L., R. P. Lin, C. Mazelle, H. Rème, P. A. Cloutier, J. E. P. Connerney, M. H. Acuña, and N. F. Ness (2001), Probing Mars' crustal magnetic field and ionosphere with the MGS electron reflectometer, *J. Geophys. Res.*, *106*, 23,419–23,428.
Nicholson, W. P., G. Gronoff, J. Lilensten, A. D. Aylward, and C. Simon (2009), A fast computation of the secondary ion production in the ionosphere of Mars, *Mon. Not. R. Astron. Soc.*, *400*, 369–382.
Opal, C. B., W. K. Peterson, and E. C. Beaty (1971), Measurements of Secondary-Electron spectra produced by electron impact ionization of a number of simple gases, *J. Chem. Phys.*, *55*, 4100–4106.
Peterson, W. K., E. N. Stavros, P. G. Richards, P. C. Chamberlin, T. N. Woods, S. M. Bailey, and S. C. Solomon (2009), Photoelectrons as a tool to evaluate spectral variations in solar EUV irradiance over solar cycle timescales, *J. Geophys. Res.*, *114*, A10304, doi:10.1029/2009JA014362.
Porter, H. S., F. Varosi, and H. G. Mayr (1987), Iterative solution of the multistream electron transport equation, 1. Comparison with laboratory beam injection experiments, *J. Geophys. Res.*, *92*(A6), 5933–5959, doi:10.1029/JA092iA06p05933.
Rees, M. H., A. I. Stewart, and J. C. G. Walker (1969), Secondary electrons in aurora, *Planet. Space Sci.*, *17*, 1997–2008.
Richards, P. G., J. A. Fennelly, and D. G. Torr (1994a), EUVAC: A solar EUV flux model for aeronomic calculations, *J. Geophys. Res.*, *99*(A5), 8981–8992, doi:10.1029/94JA00518.
Richards, P. G., J. A. Fennelly, and D. G. Torr (1994b), Correction to "EUVAC: A solar EUV flux model for aeronomic calculations" [Journal of Geophysical Research, 99, 8981–8992 (1994)], *J. Geophys. Res.*, *99* (A7), 13,283, doi:10.1029/94JA01446.
Richards, P. G., T. N. Woods, and W. K. Peterson (2006), HEUVAC: A new high resolution solar EUV proxy model, *Adv. Space Res.*, *37*(2), 315–322, doi:16/j.asr.2005.06.031.
Schunk, R. W., and A. F. Nagy (1978), Electron temperatures in the *F* region of the ionosphere: Theory and observations, *Rev. Geophys.*, *16*(3), 355–399, doi:10.1029/RG016i003p00355.
Schunk, R. W., and A. F. Nagy (2004), *Ionospheres: Physics, Plasma Physics, and Chemistry*, 554 pp., Cambridge Univ. Press, New York.
Shirai, T., T. Tabata, and H. Tawara (2001), Analytic cross sections for electron collisions with CO, CO_2, and H_2O relevant to edge plasma impurities, *At. Data Nucl. Data Tables*, *79*, 143–184.
Shirai, T., T. Tabata, H. Tawara, and Y. Itikawa (2002), Analytic cross sections for electron collisions with hydrocarbons: CH_4, C_2H_6, C_2H_4, C_2H_2, C_3H_8, and C_3H_6, *At. Data Nucl. Data Tables*, *80*, 147–204.
Simon, C., O. Witasse, F. Leblanc, G. Gronoff, and J. Bertaux (2009), Dayglow on Mars: Kinetic modelling with SPICAM UV limb data, *Planet. Space Sci.*, *57*, 1008–1021.
Simon Wedlund, C., G. Gronoff, J. Lilensten, H. Ménager, and M. Barthélemy (2011), Comprehensive calculation of the energy per ion pair or w values for five major planetary upper atmospheres, *Ann. Geo.*, *29*(1), 187–195, doi:10.5194/angeo-29-187-2011.
Smith, F. L., and C. Smith (1972), Numerical evaluation of Chapman's grazing incidence integral ch (X, $_{\mathrm{chi}}$), *J. Geophys. Res.*, *77*(19), 3592–3597, doi:10.1029/JA077i019p03592.
Stamnes, K., S. Tsay, K. Jayaweera, and W. Wiscombe (1988), Numerically stable algorithm for discrete-ordinate-method radiative transfer in multiple scattering and emitting layered media, *Appl. Opt.*, *27*, 2502–2509.
Stolarski, R. S. (1972), Analytic approach to photoelectron transport, *J. Geophys. Res.*, *77*(16), 2862–2870, doi:10.1029/JA077i016p02862.
Straub, H. C., P. Renault, B. G. Lindsay, K. A. Smith, and R. F. Stebbings (1996), Absolute partial cross sections for electron-impact ionization of H_2, N_2, and O_2 from threshold to 1000 eV, *Phys. Rev. A*, *54*, 2146–2153, doi:10.1103/PhysRevA.54.2146.
Swartz, W. E., J. S. Nisbet, and A. E. S. Green (1971), Analytic expression for the energy-transfer rate from photoelectrons to thermal-electrons, *J. Geophys. Res.*, *76*(34), 8425–8426, doi:10.1029/JA076i034p08425.
Tabata, T., T. Shirai, M. Sataka, and H. Kubo (2006), Analytic cross sections for electron impact collisions with nitrogen molecules, *At. Data Nucl. Data Tables*, *92*, 375–406.
Torr, M. R., and D. G. Torr (1985), Ionization frequencies for solar cycle 21: Revised, *J. Geophys. Res.*, *90*(A7), 6675–6678, doi:10.1029/JA090iA07p06675.
Whitten, R. C., and L. Colin (1974), The ionospheres of Mars and Venus, *Rev. Geophys. 12*(2), 155–192, doi:197410.1029/RG012i002p00155.
Witasse, O., T. Cravens, M. Mendillo, J. Moses, A. Kliore, A. F. Nagy, and T. Breus (2008), Solar system ionospheres, *Space Sci. Rev.*, *139*, 235–265.
Withers, P. (2009), A review of observed variability in the dayside ionosphere of Mars, *Adv. Space Res.*, *44*(3), 277–307, doi:16/j.asr.2009.04.027.
Woods, T. N., S. M. Bailey, W. K. Peterson, S. C. Solomon, H. P. Warren, F. G. Eparvier, H. Garcia, C. W. Carlson, and J. P. McFadden (2003), Solar extreme ultraviolet variability of the x-class flare on 21 April 2002 and the terrestrial photoelectron response, *Space Weather*, *1*(1), 1001, doi:10.1029/2003SW000010.
Woods, T. N., F. G. Eparvier, S. M. Bailey, P. C. Chamberlin, J. Lean, G. J. Rottman, S. C. Solomon, W. K. Tobiska, and D. L. Woodraska (2005), Solar EUV experiment (SEE): Mission overview and first results, *J. Geophys. Res.*, *110*, A01312, doi:10.1029/2004JA010765.

G. Gronoff and C. J. Mertens, Chemistry and Dynamics Branch, Science Directorate, NASA Langley Research Center, Mail Stop 401B, 21 Langley Blvd., Hampton, VA 23681-2199, USA. (Guillaume.P.Gronoff@nasa.gov)
R. J. Lillis, Space Sciences Laboratory, University of California Berkeley, 7 Gauss Way, Berkeley, CA 94720, USA.
C. Simon Wedlund, Belgian Institute for Space Aeronomy (BIRA-IASB), Ave. Circulaire 3, B-1180 Brussels, Belgium.